Nanoscale

Accepted Manuscript

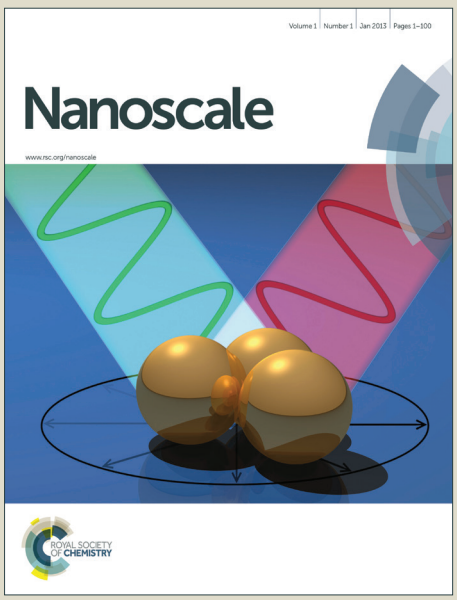

ROYAL SOCIETY OF CHEMISTRY

www.rsc.org/nanoscale

Cite this: DOI: 10.1039/c0xx00000x

www.rsc.org/xxxxxx

ARTICLE TYPE

Creation of nanopores on graphene planes with MgO template for preparing high-performance supercapacitor electrode

Huanjing Wang, Xiuxia Sun, Zonghuai Liu and Zhibin Lei*

Received (in XXX, XXX) Xth XXXXXXXXX 20XX, Accepted Xth XXXXXXXXX 20XX

DOI: 10.1039/b000000x

Creation of nanopores on graphene planar sheets is of great significance in promoting the kinetic diffusion of electrolyte and enhancing the utilization efficiency of graphene planar sheets. Herein, we developed a facile chemical vapor deposition strategy to prepare highly porous graphene with flake-like MgO as template and ferrocene as the carbon precursor. The graphene layers show highly porous structure with small mesopores of 4-8 nm, large mesopore of 10-20 nm and additional macropores of 100-200 nm. These nanopores on graphene sheets provide numerous channels for fast ion transport perpendicular to the 2D basal plane, while the good powder conductivity ensures an effective electron propagation within 2D graphene plane. As a result, a specific capacitance of 303 F g^{-1}, an areal capacitance up to 17.3 μF cm^{-2} and a nearly tenfold shorter time constant were achieved when compared with those of nonporous and stacked graphene electrode. The method demonstrated herein would open up opportunity to prepare porous graphene for a wide applications in energy storage, biosensor, nanoelelctronics and catalysis.

Introduction

Electrochemical capacitors, also known as supercapacitors, represent one of the promising energy storage devices that store energy through fast ion adsorption or highly reversible Faradic redox reaction at the electrode/electrolyte interface.[1-3] With the unique features like long life cycle, fast charging/discharging rate and high specific power density, supercapacitors have found wide applications as energy supplies in uninterruptible power, high power electronic devices or hybrid electric vehicles.[2] However, for most of their practical applications, supercapacitors store much less energy as compared with lithium ion batteries. Thus, great efforts have been devoted to improve the energy density of a supercapacitor through optimizing the pore textures of electrode materials to increase their specific capacitances or through widening the working voltage by configuring an asymmetric supercapacitor or using a non-aqueous electrolyte.[4-6]

The overall performance of a supercapacitor is strongly affected by the property and microstructure of the electrode materials. Carbon materials with various morphologies have been extensively investigated as supercapacitor electrode because of their structure advantages including good conductivities, excellent chemical stability, controllable porosity and tailored surface physicochemical properties.[7,8] In particular, graphene, consisting of single-layer of sp^2 carbon atoms covalently bonded in 2D basal plane, has received particular attentions for electrochemical energy storage due to its excellent mechanical and electronic properties as well as the exceptionally high surface area.[9-13] Although the chemical or thermal reduction of exfoliated graphene oxides (GO) represents one of the promising route toward mass production of graphene-based materials,[14,15] the strong sheet-to-sheet van der Waals interaction leads to a severe layer restacking, which not only greatly reduces the ion-accessible surface area, but also brings a large ion diffusion resistance between the adjacent graphene layers.

To improve the kinetic diffusion of electrolyte, three-dimensional (3D) graphene architecture with interconnected pore structure like foam, sponges and aerogels have been developed through hydrothermal reduction, chemical vapor deposition, freeze-drying and covalently interconnection.[16-23] These 3D graphene frameworks with micrometer-sized macropores have successfully applied as the attractive and robust matrixes for accommodating other pseudocapacitive components.[24-27] As the textural micrometer-sized macropores were primarily formed by random arrangement of the individual graphene sheets, these graphene networks actually exhibited rather low specific surface area and unsatisfied overall capacitive performancee. On the other hand, to improve the electrochemically active surface area, various carbon materials have been successfully intercalated between graphene sheets to preclude the severe sheets restacking.[28-30] In particular, porous carbons with reduced particle size and short ion channels have demonstrated to be the excellent spacers to significantly improve the overall capacitance performance of composite electrode.[28,31] However, transport of electrolyte in such cases is limited within the in-plane graphene layers, while the ion diffusion perpendicular to the graphene basal plane is usually forbidden due to the absent of ion pathway on graphene sheets. Most recently, porous graphene with specific surface area up to 3100 m^2 g^{-1} was achieved by chemical activation of microwave exfoliated graphene oxides (MEGO)

with KOH.[32,33] The structural nanopores on the graphene basal plane led to an excellent capacitive performance with a specific capacitance up to 166 F g^{-1} in ionic liquid electrolyte.[32] This result clearly demonstrates that the structural porosity is of great significance in promoting the access of electrolyte to the interior surface. However, creation of such nanopores on graphene sheets yet remains a great challenge in nanoscience and technology.[34]

Apart from the 3D skeleton of nickel foam, porous MgO and layered double hydroxides have also been explored as solid scaffolds to grow graphene-like materials.[35-38] The microstructures and physicochemical properties of the final graphene products strongly depends on the macroscopic morphology of the initial inorganic templates as well as the selecting of carbon precursors. Our previous findings have demonstrated that the pyrolysis of ferrocene on silica substrates tends to form carbon film with few-layer thickness.[39,40] Inspired by these results, herein we report an highly porous graphene material that was prepared by chemical vapor deposition of ferrocene on porous MgO flake. The small mesopores of 4-8 nm and the large mesopore of 10-20 nm, along with the macropores of 100-200 nm on the less-stacking graphene sheets substantially promote the kinetic electrolyte transport perpendicularly to the basal plane of the adjacent graphene layers. Meanwhile, these pores enables a sufficient utilization of graphene surface for electrochemical energy storage, yielding an areal specific capacitance up to 17.3 μF cm^{-2}. The high capacitive performance and the good cycling capability in both aqueous and non-aqueous electrolyte make this porous graphene materials very attractive as high-performance electrode materials for supercapacitor applications.

Experimental

Sample preparation

The flake-like magnesium hydroxide carbonate was prepared by a modified method as described previously.[41] Typically, 4.61 g of $Mg(NO_3)_2$ $6H_2O$ and 21.62 g of urea were dissolved in 120 mL water. The solution was heated to 100 ℃ and refluxed under continuous magnetic stirring for 12 h, followed by keeping at 95 ℃ statically for another 12 h. The product was collected by filtration, rinsed with copious water and ethanol and drying at 80 ℃. The subsequent calcinations of magnesium hydroxide carbonate in air at 500 ℃ for 60 min converted it into flake-like porous magnesium oxide.

The magnesium oxide was applied as the template to grow porous graphene using a chemical vapour deposition method as described previously.[39,40] Typically, about 0.2 g of calcinated MgO powder was loaded on a quartz boat, which was placed in the center of a quartz tube heated by a furnace. The sublimation and the pyrolysis of the ferrocene were conducted in N_2 flow at 120 and 500 ℃, respectively. After 60 min of CVD, the graphene-MgO composite was subjected to annealing in flowing N_2 at 800 ℃ for 90 min. Finally, the obtained graphene-MgO composite was treated with hot HCl solution (150 mL of 2.0 mol L^{-1}) to etch away the MgO template. The porous graphene was collected by filtration, washing with copious deionized water and ethanol, and dried at 80 ℃. This typical recipe could yield porous graphene of ~30 mg. The optimized experiment results indicated that if the CVD duration was shorter than 30 min, it is hardly to get the products. On the other hand, longer CVD duration over 60 min will decrease the specific surface area of the porous graphene due to the increased layer thickness.

Characterization

The morphology of the samples was observed by field-emission scanning electron microscopy (FESEM) on FEI Quanta 600F equipped with an energy dispersive spectrum (EDS) analyzing system. The microstructure of the samples was examined on a JEOL-2100F HRTEM at an acceleration voltage of 200 kV. Nitrogen adsorption/desorption isotherms were measured at 77 K on Quantachrome SI-3 analyzer. Samples were degassed at 180 ℃ for 6 h prior to the measurement. The specific surface areas of the samples were calculated using the Brunauer-Emmett-Teller (BET) method with the adsorption data at the relative pressure (P/Po) range of 0.05–0.2. The total pore volumes were estimated at P/Po = 0.99. The pore size distribution (PSD) curves were calculated from the adsorption branch using the nonlocal density functional theory (NLDFT) model assuming the slit pore geometry. X-ray photoelectron spectroscopy (XPS) spectra were collected on an AXIS ULTRA spectrometer (Kratos Analytical) using a monochromatized Al Ka X-ray source (1486.71 eV). Raman spectra were collected on a Renishaw inVia Raman microscope with an excitation wavelength of 532 nm. The electrical conductivity of sample was measured by a four-point probe method. The sample were pressed into a thin disk under a pressure of 2.5 MPa cm^{-2}.

Electrochemical measurements

The working electrode was prepared by mixing an active material (90 wt%) with carbon black (5 wt%) and polytetrafluoroethylene (PTFE, 5 wt%) in water. The slurry of the mixture was then painted between two pieces of nickel foam (1 cm^2) and pressed under a pressure of 500 kg cm^{-2}. The mass loading for each electrode is typical of ~1.8 mg cm^{-2}, which yields an electrode with thickness about ~40 μm and density of ~0.5 g cm^{-3}. The electrochemical measurement was carried out using both three-electrode and two electrode configuration, with 6.0 mol L^{-1} aqueous KOH and 1.0 mol L^{-1} tetraethylammonium tetrafluoroborate ($TEABF_4$) in acetonitrile (AN) as electrolyte. In a three-electrode cell, Pt wire and Ag/AgCl electrode were used as the count electrode and the reference electrodes, respectively. While in a two-electrode configuration, a Swagelock-type cell with two symmetric working electrodes was configured and Celgard® 3501 membrane was used as the separator. The electrochemical performance of the electrode materials was characterized by cyclic voltammetry (CV), galvanostatic charge-discharge and electrochemical impedance spectroscopy (EIS) on an CHI 660D (Chenhua, Shanghai) electrochemical workstation. The total capacitance of a supercapacitor was calculated from the galvanostatic discharge process according to the following equation: $C_{total} = I \times \Delta t/(\Delta V \times m)$, where I is the discharge current (A), Δt is the discharge time (s), ΔV is the voltage change (V) excluding the IR drop during the discharge process, and m is the total mass of the active material for both electrodes (g). The specific capacitance of the single electrode is thus calculated as $Cs = 4 \times C_{total}$. The energy density (E) and the power density (P) were calculated based on the following equations: $E = 1/2C_{total}V^2$,

$P = E/t$, where C_{total} is the total capacitance of two-electrode cell (F g^{-1}), V is the voltage of the supercapacitor (V) and t is the discharge time (s). The equivalent series resistance (ESR) was calculated using the voltage drop at the beginning of discharge, Vdrop at certain current density I, according to $ESR = V_{drop}/2I$.[42] The electrochemical impedance spectroscopy (EIS) measurement of the supercapacitor was performed with amplitude of 10 mV in the frequency ranges of 5 mHz to 100 kHz.

Results and discussion

The magnesium hydroxide carbonate was prepared by a co-precipitation reaction of $Mg(NO_3)_2$ $6H_2O$ with urea at 100 ℃. The sharp XRD peaks (Fig. S1) of the product at 2θ = 9.6, 15.2 and 30.8 ° can be readily indexed to the pure phase of orthorhombic $Mg_5(CO_3)_4(OH)_2$ $4H_2O$ (JCPDS 70-1177). Calcination of the $Mg_5(CO_3)_4(OH)_2$ $4H_2O$ sample at 500 ℃ in flowing air converted it into MgO which was verified by XRD (Fig. S1) and TGA result (Fig. S2). The strong diffraction peaks of the calcinated sample at 2θ = 42.9 and 62.2 ° correspond to the (200) and (220) reflections of cubic MgO (JCPDS 78-0430), respectively. The formation of pure-phase MgO suggests the complete decomposition of $Mg_5(CO_3)_4(OH)_2$ $4H_2O$ at 500 ℃.

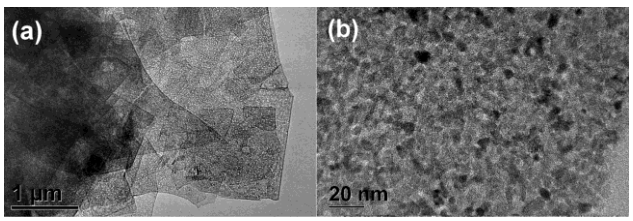

Fig. 1 TEM images of porous MgO with different magnifications.

The macroscopic morphology of the MgO was observed by SEM (Fig. S3). It is seen that MgO displays a typical flake-like morphology with lateral dimension over tens of micrometer and flake thickness of ~20 nm (Fig. S3). The TEM image of MgO clearly shows a great number of nanopores on the flakes (Fig. 1a). A magnified image reveals that these irregular mesopores with pore size of 3-8 nm was actually formed by the voids of MgO particles (Fig. 1b). According to the TGA result, these voids were most likely caused by the gaseous CO_2 and H_2O molecules that were released during the thermal decomposition of $Mg_5(CO_3)_4(OH)_2$ $4H_2O$ at 500 ℃. This assumption was verified by comparing the TEM images before and after calcinations (Fig. 1 and Fig. S4). Meanwhile, an evident increase of specific surface area from 25 to 41 m^2 g^{-1} and pore volume from 0.11 to 0.16 cm^3 g^{-1} after calcinations also supports this assumption (Table S1).

The porous flake-like MgO was used as sacrificial template to grow porous graphene. Fig. 2a presents the morphology of the graphene-MgO composite. Besides the similar flake-like morphology, a great number of particles with size of ~20 nm were found to be homogeneously distributed on the composite surface. Given that the pyrolysis of ferrocene at elevated temperature yields both carbon and FeO*x* particles,[43] these particles is likely due to the deposited FeO*x* particles during CVD process. The element compositions and their distributions on the graphene-MgO composite were examined by EDS elemental mapping. As shown in Fig 2c-f, the element C, Mg, Fe and O were detected and uniformly dispersed on the surface of whole

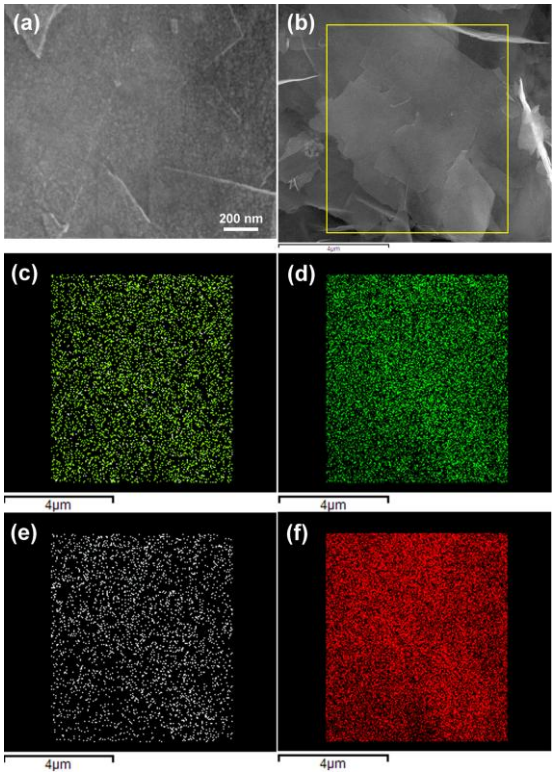

Fig. 2 FESEM (a), STEM (b) images of graphene-MgO composite and its corresponding elemental mappings of C (c), O (d), Fe (e), Mg (f).

composite matrices. These results verify the formation of carbon and FeO_x on the MgO surface.

However, quite different from the rigid graphene-MgO flake as shown in Fig. 3a, the isolated graphene sheets after dissolving MgO and FeO_x with hot HCl solution exhibits a high flexibility with individual sheets scattered in random orientations (Fig. 3b and 3c). It is noteworthy that the curved paper-like graphene with continuous silk veil wave is in sharp contrast with the aggregated

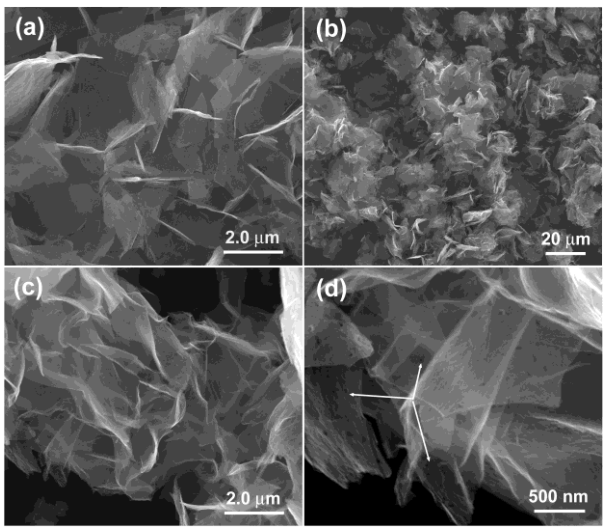

Fig. 3 FESEM images of graphene-MgO composite (a) and the isolated porous graphene (b-d) after etching away MgO template with aqueous HCl solution.

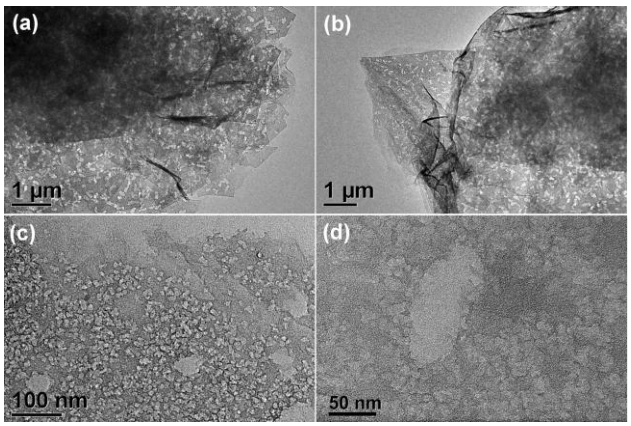

Fig. 4 TEM images of porous graphene with different magnifications.

graphene that were prepared by the conventionally chemical reduction of GO suspension.[14] Moreover, a close examination clearly shows the presence of opened holes on crumpled graphene sheets (Fig. 3d). A HRTEM shown in Fig S5 reveals a thickness of about 1.2 nm, suggesting the porous graphene consists of 3-4 graphene layers.

The microstructure of the porous graphene was examined by TEM. It is seen that the graphene were composed of many slightly overlapped platelets resembling the initial morphology of the flake-like MgO (Fig. 4a, 4b). Moreover, a great number of worm-like macropores varying from 100 to 200 nm in size were also uniformly distributed on the graphene sheets. It is interesting to note that apart from these sub-micrometer-sized macropores, a great number of small mesopores of 4-8 nm and large mesopores of 10-20 nm were also clearly seen on the magnified scopes (Fig. 4c and 4d). The porosity was further verified by N_2 adsorption. As shown in Fig. 5a, the distinct increase of N_2 uptake of porous graphene as compared with graphene-MgO composite indicates a significant increase of both surface area and pore volume. Moreover, a characteristic type IV isotherm with a pronounced hysteresis in the relative pressure (P/P_0) of 0.5-0.8 reveals the presence of large number of mesopores. A pore volume analysis shows about 68% of the total pore volume was contributed by the pores smaller than 16 nm (Fig. 5b). The corresponding NLDFT pore size distribution shows well-developed mesopores with a broad pore size distribution ranging from 2 to 8 nm (inset in Fig. 5b). These results are in good agreement with the TEM images as shown in Fig. 4c and 4d. Due to the large number of structural porosity, the graphene exhibits a specific surface area of 1754 m^2 g^{-1} and a large pore volume of 2.81 cm^3 g^{-1} (Table S1). Note this specific surface area value is even higher than that of laser-scribing graphene (1520 m^2 g^{-1}),[11] anti-solvent derived non-stacked graphene (1435.4 m^2 g^{-1}),[44] and significantly higher than that of 3D graphene network[19, 23] and most of graphene prepared by a solution-based route.[14,45] This comparison demonstrates the advantages of the present CVD route to producing highly porous graphene with large accessible surface area. It is noteworthy that these mesopores, together with the sub-micrometer-sized macropores provide opened ion channels for kinetic transport of electrolyte across the adjacent graphene sheets.

The chemical composition of the porous graphene was investigated by XPS spectroscopy. Only C 1s and O 1s signals

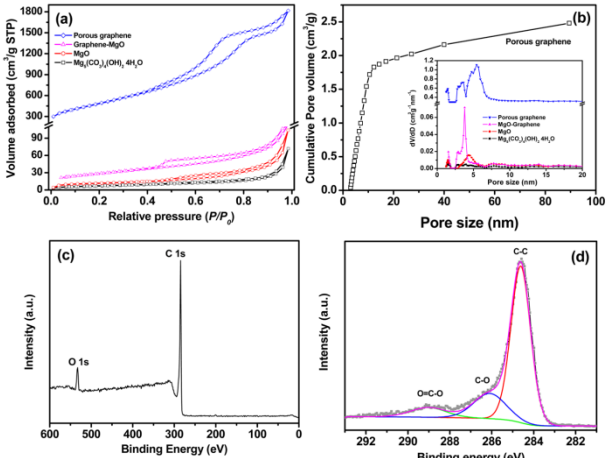

Fig. 5. N_2 adsorption isotherms (a), cumulative pore volume (b) with inset showing pore size distribution calculated from the slit/cylindrical NLDFT model, survey XPS (c) and C 1s XPS spectrum (d) of porous graphene.

were present in the survey XPS spectrum (Fig. 5c), indicating the complete removal of FeO_x species and MgO flake during the etching process. The deconvoluted C 1s spectrum gives an intensive peak at 284.6 eV, along with a weak C-O peak at 286.2 eV and a broad O=C-O peak at 289.1 eV (Fig. 5d). The atomic ratio of C/O in the porous graphene was determined to be 19 according to the quantitative XPS analysis, suggesting a high content of sp^2-bonded carbon in the product. This was also evident from the Raman spectrum as shown in Fig. S6. Two fundamental bands at 1340 (D band) and 1589 cm^{-1} (G band) were clearly observed, which correspond to the disordered sample or graphene edge, and the first-order scattering of E_{2g} mode of sp^2 carbon domains, respectively. The relatively strong G band is indicative of more sp^2 domains in graphene basal plane. However, this G band is relatively low in intensity with respect to that of graphene nanomesh catalytically grown on Cu nanoparticles.[46] Moreover, the occurrence of two broad band centered at 2710 and 2880 cm^{-1} demonstrates that our porous graphene is structurally similar to the chemically converted graphene (CCG) through thermal annealing under different conditions.[47,48] This comparison demonstrates that there was a substantial number of defects on graphene plane which might be caused by the high porosity as well as the small amount of residual oxygen-containing functionalities. As a result, the powder conductivity was determined to be 188 S m^{-1} by a four-point probe method.

The porous graphene was applied as supercapacitor electrode and its electrochemical performance was evaluated by a three-electrode cell with 6.0 mol L^{-1} KOH solution as aqueous electrolyte. Fig. S7a shows the CV profiles of porous graphene electrode at different scan rates. The rectangular CV profiles with negligible contribution from pseudocapacitance is in consistence with the low level of surface oxygen functional groups (below 5 at% based on XPS analysis). The galvanostatic charge-discharge curves of porous graphene electrode measured at different current densities was presented in Fig. S7b. The triangular charge-discharge curves are characteristic of electrical double-layer capacitance (EDLC) arising from the electro-adsorption of ion on

Cite this: DOI: 10.1039/c0xx00000x

www.rsc.org/xxxxxx

ARTICLE TYPE

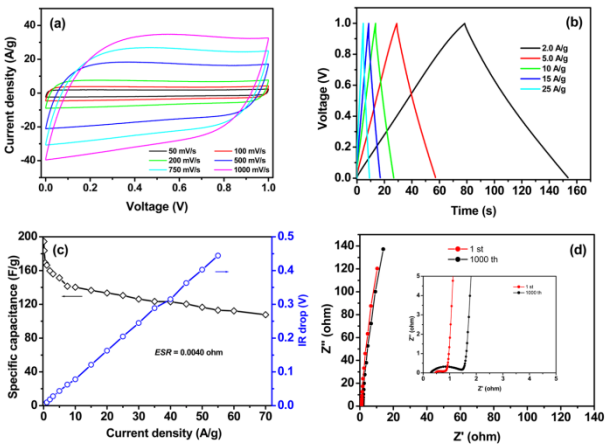

Fig. 6 Capacitive performance of two-electrode capacitor with porous graphene as symmetric electrode and 6.0 mol L^{-1} KOH as aqueous electrolyte. (a) CV profiles at different scan rates, (b) galvanostatic charge-discharge curves at different current densities, (c) variation of specific capacitance and IR drop against current density, and (d) Nyquist plots of porous graphene materials before and after 1000 cycles.

electrode surface. It is noted that the specific capacitance of porous graphene reach 303 F g^{-1} at constant current density of 0.5 A g^{-1}, which is higher than 255 F g^{-1} of nanomesh graphene[38] and outperforms most of graphene electrode with typical capacitance value of 100-250 F g^{-1} in aqueous electrolyte (Table S2).[14,34,49-51] The areal capacitance normalized by specific surface area reaches 17.3 μF cm^{-2}, also much higher than 10-15 μF cm^{-2} of nanomesh graphene[38] and most of other porous carbon electrode.[52,53] Considering the maximum EDLC of ~20 μF cm^{-2} delivered by carbon-based electrodes[8] and the negligible contribution of pseudocapacitance from surface oxygen functionalities, the high areal capacitance of 17.3 μF cm^{-2} demonstrates that over 85% planar surface can be facilely accessed by the electrolyte. Such a high utilization efficiency is evidently ascribed to the crumbled graphene sheets with large number of nanopores, enabling the inaccessible surface of stacked graphene to be fully utilized for effective charge storage.

To get more reliable capacitive performance, a two-electrode cell with symmetric porous graphene electrode was configured with 6.0 mol L^{-1} KOH as aqueous electrolyte. It is seen that even at very high scan rate of 1.0 V s^{-1}, the porous graphene electrode still remains a rather rectangular CV curve (Fig. 6a). Whereas, an obviously distorted CV curves were observed at scan rate of 300 mV s^{-1} for the aggregated graphene oxide reduced by urea.[14] The galvanostatic charge-discharge curves at different current densities shows nearly linear slops with negligible IR drop (Fig. 6b), suggesting a low internal resistance and an ideal capacitive behavior. The variation of IR drop with the current density was plotted in Fig. 6c. An extremely small equivalent series resistance (ESR) of 0.004 ohm coincides with the negligible IR drop at high current density, further confirming a very low internal resistance.

From the discharge curves, the specific capacitance at constant current density of 0.1 A g^{-1} was calculated to be 196 F g^{-1}. Most importantly, as the discharging current increased 700-fold from 0.1 to 70 A g^{-1}, the capacitance still preserved a high value of 108 F g^{-1} (Fig. 6c). Such excellent rate capability is indispensable for practical applications of a high-rate supercapacitor. However, given that the potential range applied in a symmetric two electrode cell is markedly different from that in the three electrode cell,[54] this specific capacitance value is smaller than that measured from three-electrode system. Nevertheless, the high-rate performance exhibited by the porous graphene is closely related to its unique structure that integrating mesopores, sub-micrometer pores with good electronic conductivity, promoting a fast electron migration within 2D plane and a rapid ion transport across the adjacent graphene layers.

To demonstrate the cycling performance of the porous graphene in KOH aqueous electrolyte, we measured its specific capacitance at a constant current density of 4.0 A g^{-1} and the results were included in Fig. 7f. It is seen that the porous graphene electrode remains a stable electrochemical stability and preserved 96% of its initial specific capacitance after 1000 cycles of galvanostatic charge-discharge. The rectangular CV profiles with a slight decreased integrated area (Fig. S8) and the slightly enlarged semicircles as shown in Nyquist plots (Fig. 6d) after 1000 cycling also supports this electrochemical cyclability. The capability of porous graphene by integrating its high-rate performance with its superior cycling stability is of great importance for high-performance supercapacitor.

The capacitive performance of the porous graphene-based capacitor was also tested in 1.0 mol L^{-1} $TEABF_4$/AN electrolyte. The high-rate performance can be clearly seen from its rectangular CV behavior at high scan rate of 300 mV s^{-1} (Fig. 7a). The symmetric and linear charge-discharge profiles at an operating voltage of 0–2.5 V reveal a highly reversible charge/discharge character in a wide voltage window (Fig. 7b). As compared with the aqueous electrolyte, the capacitor in organic electrolyte displays a relatively large ESR (0.0152 ohm) and relatively low capacitance retention (dropped from 140 to 72 F g^{-1} upon increase of current density from 0.1 to 30 A g^{-1}.) (Fig. 7c). Such discrepancy can be interpreted by the low ion conductivity of AN (50-60 mS cm^{-1} *vs* 540 mS cm^{-1} of aqueous KOH),[55] and the large solvated ion sizes of $(CH_3CH_2)_4N^+$ (1.3 nm *vs* 0.334 nm of solvated K^+).[56,57]

The kinetic ion diffusion within the electrode was investigated by electrochemical impedance spectroscopy. Fig. 7d shows the dependence of impedance phase angle on the frequency of graphene electrode in two different electrolytes. The solution-based graphene with hydrazine (RGO-N_2H_4)[15] and urea (RGO-urea)[14] as reducing agents were also included for comparison purpose. The relaxation time constant τ_0 of supercapacitor, which is defined as the $1/f_0$ at a phase angle of -45 °, represents the transition between a capacitive behavior at frequency lower than $1/f_0$ and a resistive behavior at frequency

Cite this: DOI: 10.1039/c0xx00000x

www.rsc.org/xxxxxx

ARTICLE TYPE

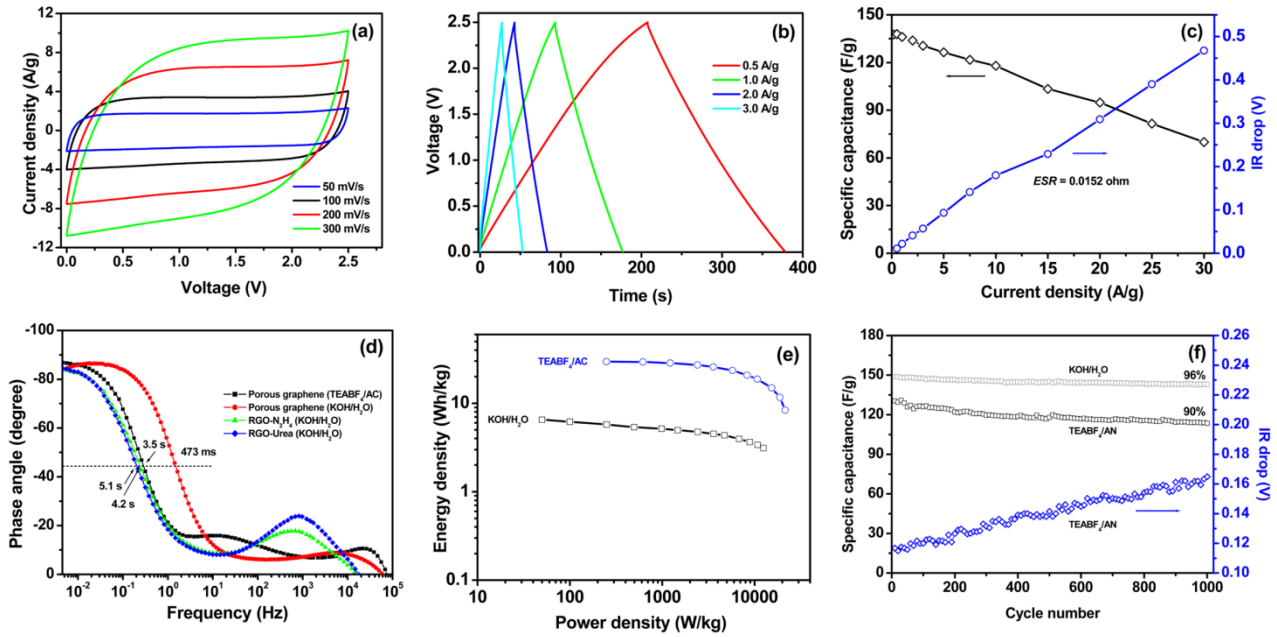

Fig. 7 (a) CV profiles at different scan rates, (b) galvanostatic charge-discharge curves at different current densities, (c) capacitance retention of porous graphene in $TEABF_4$/AN electrolyte. (d) Impedance phase angle versus frequency of different graphene electrodes, (e) Ragone plots, and (f) cycle performance of porous graphene electrode in both aqueous KOH and $TEABF_4$/AN electrolyte electrolyte at current density of 4.0 and 3.0 A g^{-1}, respectively.

higher than $1/f_0$.[58] For the porous graphene electrode, the characteristic frequencies f_0 at the phase angle of -45 ° was measured to be 2.11 Hz in aqueous KOH and 0.29 Hz in $TEABF_4$/AN electrolyte, corresponding to a time constants τ_0 (=$1/f_0$) of 473 ms and 3.5 s in aqueous KOH and $TEABF_4$/AN electrolyte, respectively. In contrast, the phase angle curves of RGO-N_2H_4 and RGO-urea in aqueous KOH show obvious shift toward low frequency range, yielding a larger time constant of 4.2 and 5.1 s, respectively (Fig. 7d). Note these time constant values are nearly tenfold longer than that of the porous graphene electrode in aqueous KOH and even longer than that of porous graphene in $TEABF_4$/AN electrolyte. Given that both RGO-N_2H_4 and RGO-urea consist of stacked graphene sheets with no ion channels on the 2D plane, the very short time constant of porous graphene highlights the significant role of these nanopores in dramatically promoting the kinetic diffusion of electrolyte in the interior of electrode.

The high-rate performance of porous graphene electrode was also manifested in its Ragone plot (Fig. 7e). It is clearly seen that the energy density does not show dramatic drop with the increase of the power density in both aqueous and organic electrolyte. Because the energy density of a supercapacitor strongly depends on its working voltage, the wide voltage window of $TEABF_4$ in acetonitrile affords the porous graphene-based capacitor a much high energy density. As shown in Fig. 7e, the porous graphene electrode delivery an energy of 29.6 Wh kg^{-1} at power density of 250 W kg^{-1}, which is in sharp contrast with 6.5 Wh kg^{-1} in aqueous KOH electrolyte. Even at a high power density of 18.8 kW kg^{-1}, the capacitor still delivery an energy of 11.7 Wh kg^{-1}, in good agreement with its rectangular CV profile at high scan rate and good capacitance retention at high changing/discharge rate. These excellent capacitive characters are closely related to its rather low ESR which is ascribed to the fast ion diffusion and rapid charge transfer due to the present of great number of nanopores on the highly conductive graphene sheets.

Fig. 7f shows the cycling performance of the porous graphene electrode in $TEABF_4$/AN electrolyte at a current density of 3.0 A g^{-1}. It is seen that the total capacitance displays a slight decrease with the cycling number. The IR drop of the capacitor was found to increase from 0.12 to 0.16 V during the 1000 cycles. This small amplitude change might be related to a loose contact between the current collector and the active materials during cycling. Actually, we examined the electrode after cycling experiment and found that a small portion of carbon powder was dropped from the current collector. Such a loose contact between graphene materials and current collector might be related to a low binder amount (PTFE, 5 wt%) in the electrode preparation. Despite the symmetric charge-discharge curves (Fig. S9), only 90% of its initial specific capacitance was preserved after 1000 continuous cycles. It should be noted that capacitance retention of 90% is much lower than the expected value for an ideal electrical double-layer capacitor. Nevertheless, the reversible charge-discharge character of the porous graphene-based supercapacitor in $TEABF_4$/AN ensures a high energy density for electrochemical

energy storage device, although underlying factors that affect the cyclability, including tailoring the surface functionality of electrode materials and optimizing the electrode fabrication technique, need to be further clarified.

Conclusions

Highly porous graphene with few-layer thickness and a specific surface area up to 1754 m^2 g^{-1} has been successfully prepared through a CVD method with ferrocene as the carbon precursor and porous MgO as sacrificial template. The good sheets conductivity offers a fast electron propagation along 2D plane, while the mesopore and the additional macropore on graphene sheets provides opened ion pathway for rapid electrolyte transport perpendicular to adjacent graphene layers, allowing for a high utilization efficiency of graphene basal plane for charge accumulation. As a result, a specific capacitance up to 303 F g^{-1}, a high-rate performance and a good electrochemical cyclability were achieved in both aqueous KOH and $TEABF_4$/AN electrolyte. These superior capacitive behavior make porous graphene one of very attractive candidates for emerging applications in biosensor, nanoelelctronics, solar cells and catalysis.

Acknowledgements

This work was financially supported by the National Nature Science Foundations of China (Grant no. 21373134), Fundamental Research Funds for the Central Universities (Grant No: GK201102002, GK201101003, GK201301002) and the Program for Key Science & Technology Innovation Team (2012KCT-21) and Nature Science Foundation of Shaanxi Province (2013JM2001).

Notes and references

School of Materials Science and Engineering, Shaanxi Normal University, 199 South Chang'an Road, Xi'an, Shaanxi, 710062, China, Email: zblei@snnu.edu.cn; Tel: 86-29-81530810; Fax: 86-29-81530702

† TGA curve, SEM and XRD patterns of MgO, TEM image of Mg5(CO3)4(OH)2 4H2O, HRTEM, Raman spectrum of porous graphene, and its electrochemical performance including CV and galvanostatic charge-discharge curves in three-electrode cell with 6.0 mol/L aqueous KOH as electrolyte, comparative electrocapacitive performances of graphene materials prepared by various methods, CV behaviors of porous graphene in two-electrode cell and the last 10 cycles in 1000 charge-discharge cycles in 1.0 mol L–1 TEABF4/AN electrolyte. See DOI: 10.1039/b000000x/

Reference

1. P. Simon and Y. Gogotsi, *Nat. Mater.*, 2008, **7**, 845.
2. J. R. Miller and P. Simon, *Science*, 2008, **321**, 651.
3. P. Simon and Y. Gogotsi, *Acc. Chem. Res.*, 2013, **46**, 1094.
4. C. Liu, Z. Yu, D. Neff, A. Zhamu and B. Z. Jang, *Nano Lett.*, 2010, **10**, 4863.
5. J. Zhang and X. S. Zhao, *ChemSusChem*, 2012, **5**, 818.
6. Z. Lei, J. Zhang and X. S. Zhao, *J. Mater. Chem.*, 2012, **22**, 153.
7. L. L. Zhang and X. S. Zhao, *Chem. Soc. Rev.*, 2009, **38**, 2520.
8. A. G. Pandolfo and A. F. Hollenkamp, *J. Power Sources*, 2006, **157**, 11.
9. R. Ruoff, *Nat. Nanotechnol.*, 2008, **3**, 10.
10. Y. Huang, J. Liang and Y. Chen, *Small*, 2012, **8**, 1805.
11. M. F. El-Kady, V. Strong, S. Dubin and R. B. Kaner, *Science*, 2012, **335**, 1326.
12. J. Chen, C. Li and G. Shi, *The Journal of Physical Chemistry Letters*, 2013, 1244.
13. C. Xu, B. Xu, Y. Gu, Z. Xiong, J. Sun and X. S. Zhao, *Energy Environ. Sci.*, 2013, **6**, 1388.
14. Z. Lei, L. Lu and X. S. Zhao, *Energy Environ. Sci.*, 2012, **5**, 6391.
15. D. Li, M. B. Muller, S. Gilje, R. B. Kaner and G. G. Wallace, *Nat. Nanotechnol.*, 2008, **3**, 101.
16. X. Cao, Y. Shi, W. Shi, G. Lu, X. Huang, Q. Yan, Q. Zhang and H. Zhang, *Small*, 2011, **7**, 3163.
17. J. Chen, K. Sheng, P. Luo, C. Li and G. Shi, *Adv. Mater.*, 2012, **24**, 4569.
18. S. Yin, Z. Niu and X. Chen, *Small*, 2012, **8**, 2458.
19. Z. Chen, W. Ren, L. Gao, B. Liu, S. Pei and H.-M. Cheng, *Nat Mater*, 2011, **10**, 424.
20. Y. Xu, K. Sheng, C. Li and G. Shi, *ACS Nano*, 2010, **4**, 4324.
21. C. Wu, X. Huang, G. Wang, L. Lv, G. Chen, G. Li and P. Jiang, *Adv. Funct. Mater.*, 2013, **23**, 506.
22. Z. Niu, J. Chen, H. H. Hng, J. Ma and X. Chen, *Adv. Mater.*, 2012, **24**, 4144.
23. P. M. Sudeep, T. N. Narayanan, A. Ganesan, M. M. Shaijumon, H. Yang, S. Ozden, P. K. Patra, M. Pasquali, R. Vajtai, S. Ganguli, A. K. Roy, M. R. Anantharaman and P. M. Ajayan, *ACS Nano*, 2013, **7**, 7034.
24. B. G. Choi, M. Yang, W. H. Hong, J. W. Choi and Y. S. Huh, *ACS Nano*, 2012, **6**, 4020.
25. J. Ji, L. L. Zhang, H. Ji, Y. Li, X. Zhao, X. Bai, X. Fan, F. Zhang and R. S. Ruoff, *ACS Nano*, 2013, **7**, 6237.
26. X.-C. Dong, H. Xu, X.-W. Wang, Y.-X. Huang, M. B. Chan-Park, H. Zhang, L.-H. Wang, W. Huang and P. Chen, *ACS Nano*, 2012, **6**, 3206.
27. Y. He, W. Chen, X. Li, Z. Zhang, J. Fu, C. Zhao and E. Xie, *ACS Nano*, 2013, **7**, 174.
28. Z. B. Lei, N. Christov and X. S. Zhao, *Energy Environ. Sci.*, 2011, **4**, 1866.
29. J. Yan, T. Wei, B. Shao, F. Ma, Z. Fan, M. Zhang, C. Zheng, Y. Shang, W. Qian and F. Wei, *Carbon*, 2010, **48**, 1731.
30. L. Qiu, X. Yang, X. Gou, W. Yang, Z.-F. Ma, G. G. Wallace and D. Li, *Chem. Eur. J.*, 2010, **16**, 10653.
31. Z. Lei, Z. Liu, H. Wang, X. Sun, L. Lu and X. S. Zhao, *J. Mater. Chem. A*, 2013, **1**, 2313.
32. Y. W. Zhu, S. Murali, M. D. Stoller, K. J. Ganesh, W. W. Cai, P. J. Ferreira, A. Pirkle, R. M. Wallace, K. A. Cychosz, M. Thommes, D. Su, E. A. Stach and R. S. Ruoff, *Science*, 2011, **332**, 1537.
33. L. L. Zhang, X. Zhao, M. D. Stoller, Y. Zhu, H. Ji, S. Murali, Y. Wu, S. Perales, B. Clevenger and R. S. Ruoff, *Nano Lett.*, 2012, **12**, 1806.
34. Z.-S. Wu, Y. Sun, Y.-Z. Tan, S. Yang, X. Feng and K. Müllen, *J. Am. Chem. Soc.*, 2012, **134**, 19532.
35. Z. Fan, Y. Liu, J. Yan, G. Ning, Q. Wang, T. Wei, L. Zhi and F. Wei, *Adv. Energy Mater.*, 2012, **2**, 419.
36. J. Sun, H. Liu, X. Chen, D. G. Evans, W. Yang and X. Duan, *Chem. Commun.*, 2012, **48**, 8126.
37. M.-Q. Zhao, X.-F. Liu, Q. Zhang, G.-L. Tian, J.-Q. Huang, W. Zhu and F. Wei, *ACS Nano*, 2012, **6**, 10759.
38. G. Ning, Z. Fan, G. Wang, J. Gao, W. Qian and F. Wei, *Chem. Commun.*, 2011, **47**, 5976.
39. Z. B. Lei, S. Y. Bai, Y. Xiao, L. Q. Dang, L. Z. An, G. N. Zhang and Q. Xu, *J. Phys. Chem. C*, 2008, **112**, 722.
40. Z. B. Lei, N. Christov, L. L. Zhang and X. S. Zhao, *J. Mater. Chem.*, 2011, **21**, 2274.
41. M.-Q. Zhao, Q. Zhang, X.-L. Jia, J.-Q. Huang, Y.-H. Zhang and F. Wei, *Adv. Funct. Mater.*, 2010, **20**, 677.
42. T. Kim, G. Jung, S. Yoo, K. S. Suh and R. S. Ruoff, *ACS Nano*, 2013, **7**, 6899.
43. Z. Lei, S. Bai, L. Dang, H. Xia, Q. Xu, Y. Cao, L. An, M. Zhao, A.-Y. Lo and S.-B. Liu, *Microporous Mesoporous Mater.*, 2009, **123**, 306.
44. Y. Yoon, K. Lee, C. Baik, H. Yoo, M. Min, Y. Park, S. M. Lee and H. Lee, *Adv. Mater.*, 2013, **25**, 4437.

45. S. Stankovich, D. A. Dikin, R. D. Piner, K. A. Kohlhaas, A. Kleinhammes, Y. Jia, Y. Wu, S. T. Nguyen and R. S. Ruoff, *Carbon*, 2007, **45**, 1558.
46. J. Liu, H. Cai, X. Yu, K. Zhang, X. Li, J. Li, N. Pan, Q. Shi, Y. Luo and X. Wang, *J. Phys. Chem. C*, 2012, **116**, 15741.
47. D. Yang, A. Velamakanni, G. Bozoklu, S. Park, M. Stoller, R. D. Piner, S. Stankovich, I. Jung, D. A. Field, C. A. Ventrice Jr and R. S. Ruoff, *Carbon*, 2009, **47**, 145.
48. W. Gao, L. B. Alemany, L. Ci and P. M. Ajayan, *Nat Chem*, 2009, **1**, 403.
49. C.-M. Chen, Q. Zhang, M.-G. Yang, C.-H. Huang, Y.-G. Yang and M.-Z. Wang, *Carbon*, 2012, **50**, 3572.
50. H. Gao, F. Xiao, C. B. Ching and H. Duan, *ACS Appl. Mater. Interfaces*, 2012, **4**, 2801.
51. H. Zhang, V. V. Bhat, N. C. Gallego and C. I. Contescu, *ACS Appl. Mater. Interfaces*, 2012, **4**, 3239.
52. H. J. Liu, W. J. Cui, L. H. Jin, C. X. Wang and Y. Y. Xia, *J. Mater. Chem.*, 2009, **19**, 3661.
53. Z. B. Lei, D. Bai and X. S. Zhao, *Microporous Mesoporous Mater.*, 2012, **147**, 86.
54. M. D. Stoller and R. S. Ruoff, *Energy Environ. Sci.*, 2010, **3**, 1294.
55. A. Lewandowski and M. Galinski, *J. Power Sources*, 2007, **173**, 822.
56. K. Fic, G. Lota, M. Meller and E. Frackowiak, *Energy Environ. Sci.*, 2012, **5**, 5842.
57. J. Chmiola, C. Largeot, P. L. Taberna, P. Simon and Y. Gogotsi, *Angew. Chem. Int. Ed.*, 2008, **47**, 3392.
58. P. L. Taberna, P. Simon and J. F. Fauvarque, *J. Electrochem. Soc.*, 2003, **150**, A292.